

# Sparse Approximation of Computational Time Reversal Imaging

M. Andrecut

IBI, University of Calgary  
2500 University Drive NW, Calgary  
Alberta, T2N 1N4, Canada

## Abstract

Computational time reversal imaging can be used to locate the position of multiple scatterers in a known background medium. Here, we discuss a sparse approximation method for computational time-reversal imaging. The method is formulated entirely in the frequency domain, and besides imaging it can also be used for denoising, and to determine the magnitude of the scattering coefficients in the presence of moderate noise levels.

PACS:

02.30.Zz Inverse problems

43.60.+d Acoustic signal processing

43.60.Pt Signal processing techniques for acoustic inverse problems

43.60.Tj Wave front reconstruction, acoustic time-reversal

# 1 Introduction

Acoustic, elastic or electro-magnetic waves scattered by the inhomogeneities in the medium carry significant information, which can be used to obtain true images of the investigated domain [1]. Recently, it was shown that scattered acoustic waves can be time-reversed and focused onto their original source location through arbitrary media, using a so-called time-reversal mirror [2]. This important result shows that one can use computational time reversal imaging to identify the location of multiple point scatterers (targets) in a known background medium [3]. In this case, a back-propagated signal is computed, rather than implemented in the real medium, and its peaks indicate the existence of possible scattering targets. The current algorithms for computational time reversal imaging are based on the null subspace projection operator, obtained through the singular value decomposition of the frequency response matrix [4-9]. Here, we discuss a different approach based on a sparse approximation method. Besides imaging, this approach can be used for denoising, and to determine the magnitude of the scattering coefficients of the targets embedded in homogeneous media in the presence of moderate noise levels. The method is formulated entirely in the frequency domain, in the case where the Born approximation can be used [10]. Relevant applications are radar imaging, exploration seismics, nondestructive material testing, microwave breast imaging, ultrasound kidney stones localization, and other acoustic inverse problems [1-9].

# 2 Frequency response matrix

We consider a system consisting of an array of  $N$  transceivers (i.e. each antenna is an emitter and a receiver) located at  $x_n \in R^D$  ( $n = 1, \dots, N$ ), and a collection of  $M$  distinct scatterers (targets) with scattering coefficients  $\rho_m$ , located at  $y_m \in R^D$  ( $m = 1, \dots, M$ ) (Fig. 1). Here,  $D = 1, 2, 3$  is the dimensionality of the space. Also, we assume that the wave propagation is well approximated in the space-frequency domain  $(x, \omega)$  by the inhomogeneous Helmholtz equation:

$$[\nabla^2 + k_0^2 \eta^2(x)] \psi(x, \omega) = -s(x, \omega), \quad (1)$$

where  $\psi(x, \omega)$  is the wave amplitude produced by a localized source  $s(x, \omega)$ ,  $k_0 = 2\pi\omega/c_0 = 2\pi/\lambda$  is the wavenumber of the homogeneous background, with  $\omega$  the frequency,  $c_0$  the homogeneous background wave speed, and  $\lambda$  the wavelength. Here,  $\eta(x)$  is the index of refraction:  $\eta(x) = c_0/c(x)$ , where  $c(x)$  is the wave speed at location  $x$ . In the background we have  $\eta_0^2(x) = 1$ , while  $\eta^2(x) = 1 + \alpha(x)$ , measures the change in the wave speed at the scatterers location.

The fundamental solutions, or the Green functions, for this problem satisfy the following equations:

$$[\nabla^2 + k_0^2] G_0(x, x') = -\delta(x - x'), \quad (2)$$

$$[\nabla^2 + k_0^2 \eta^2(x)] G(x, x') = -\delta(x - x'), \quad (3)$$

for the homogeneous and inhomogeneous media, respectively. The expression of the homogeneous Green function depends on the dimension of the space as following:

$$G_0(x, x') = \frac{i}{2k_0} \exp(ik_0|x - x'|), \quad D = 1, \quad (4)$$

$$G_0(x, x') = \frac{i}{4} H_0^{(1)}(k_0|x - x'|), \quad D = 2, \quad (5)$$

$$G_0(x, x') = \frac{\exp(ik_0|x - x'|)}{4\pi|x - x'|}, \quad D = 3, \quad (6)$$

where,  $H_0^{(1)}(\cdot)$  is the zero order Hankel function of the first kind. Also, the fundamental solution  $G(x, x')$  for the inhomogeneous medium can be written in terms of that for the homogeneous one  $G_0(x, x')$  as:

$$G(x, x') = G_0(x, x') + k_0^2 \int \alpha(z) G_0(x, z) G(z, x') dz. \quad (7)$$

This is an implicit integral equation for  $G(x, x')$ . Since the scatterers are assumed to be pointlike, the regions with  $\alpha(z) \neq 0$  are assumed to be finite, and included in compact domains  $\Omega_m$  centered at  $y_m$ ,  $m = 1, \dots, M$ , which are small compared to the wavelength  $\lambda$ . Therefore we can write:

$$\alpha(z, \omega) = \sum_{m=1}^M \rho_m(\omega) \delta(z - y_m), \quad (8)$$

and consequently we obtain the Foldy-Lax equations:

$$G(x, x') \simeq G_0(x, x') + \sum_{m=1}^M \rho_m(\omega) G_0(x, y_m) G(y_m, x'). \quad (9)$$

If the scatterers are sufficiently far apart then we can neglect the multiple scattering among the scatterers ( $G(y_m, x') \simeq G_0(y_m, x')$ ) and we obtain the Born approximation of the solution:

$$G(x, x') \simeq G_0(x, x') + \sum_{m=1}^M \rho_m(\omega) G_0(x, y_m) G_0(y_m, x'). \quad (10)$$

If  $x$  corresponds to the receiver location  $x_i$ , and  $x'$  corresponds to the emitter location  $x_j$ , then we obtain:

$$G(x_i, x_j) \simeq G_0(x_i, x_j) + H_{ij}(\omega), \quad (11)$$

where

$$H_{ij}(\omega) = \sum_{m=1}^M G_0(x_i, y_m) \rho_m(\omega) G_0(y_m, x_j), \quad i, j = 1, \dots, N, \quad (12)$$

are the elements of the frequency response matrix  $H(\omega) = [H_{ij}(\omega)]$  [4-9]. The response matrix  $H(\omega)$  is obviously a complex and symmetric  $N \times N$  matrix, since the same Green function is used in both the transmission and the reception paths.

### 3 Back-propagation and imaging

An important step in computational time-reversal imaging is to determine the frequency response matrix  $H(\omega)$ . This can be done by performing a series of  $N$  simple experiments, in which a single element of the array is excited with a suitable signal  $s$  and we measure the frequency response between this element and all the other elements of the array [1-9]. In general, given the Green function of the homogeneous media  $G_0(x, x')$ , the general solution to the Helmholtz equation is the convolution:

$$\psi(x, \omega) = (G_0 * s)(x) = \int G_0(x, x')s(x', \omega)dx'. \quad (13)$$

Thus, if the  $j$  antenna emits a signal  $s_j$  then, using the convolution theorem in the Fourier domain, the field produced at the location  $r$  is  $G_0(r, x_j)s_j$ . If this field is incident on the  $m$ -th scatterer, it produces at  $r$  the scattered field  $G_0(r, y_m)\rho_m(\omega)G_0(r, x_j)s_j$ . Thus, the total wave field at location  $r$ , due to a pulse emitted by a single element at  $x_j$  and scattered by the  $M$  targets can be expressed as:

$$\psi(r, \omega) = \sum_{m=1}^M G_0(r, y_m)\rho_m(\omega)G_0(y_m, x_j)s_j. \quad (14)$$

If this field is measured at the  $i$ -th antenna we obtain:

$$\psi(x_i, \omega) = \sum_{m=1}^M G_0(x_i, y_m)\rho_m(\omega)G_0(y_m, x_j)s_j = H_{ij}(\omega)s_j. \quad (15)$$

Thus, the response matrix can be rewritten as:

$$H(\omega) = \Gamma(\omega)R(\omega)\Gamma^T(\omega), \quad (16)$$

where

$$R(\omega) = \text{diag}\{\rho_1(\omega), \dots, \rho_M(\omega)\}, \quad (17)$$

and

$$\Gamma(\omega) = [ g(y_1, \omega) \quad g(y_2, \omega) \quad \dots \quad g(y_M, \omega) ]. \quad (18)$$

Here,  $g(y_m, \omega)$  is the Green function vector associated with the  $m$ -th scatterer

$$g(y_m, \omega) = [ G_0(x_1, y_m, \omega) \quad G_0(x_2, y_m, \omega) \quad \dots \quad G_0(x_N, y_m, \omega) ]^T. \quad (19)$$

In general, the Green function vector defined as:

$$g(r, \omega) = [ G_0(x_1, r, \omega) \quad G_0(x_2, r, \omega) \quad \dots \quad G_0(x_N, r, \omega) ]^T, \quad (20)$$

expresses the response at each array element due to a single pulse emitted from  $r$ .

In the formulation of time-reversal imaging one forms the self-adjoint matrix [6]:

$$K(\omega) = H^*(\omega)H(\omega) = \overline{H}(\omega)H(\omega), \quad (21)$$

where the star denotes the adjoint and the bar denotes the complex conjugate ( $H^* = \overline{H}$ , since  $H$  is symmetric).  $\overline{H}$  is the frequency-domain version of a time-reversed response matrix, thus  $K(\omega)$  corresponds to performing a scattering experiment, time-reversing the received signals and using them as input for a second scattering experiment. Therefore, time-reversal imaging relies on the assumption that the Green function can be always calculated.

As long as the number of antenna elements exceeds the number of scatterers,  $M < N$ , the matrix  $K(\omega)$  is rank deficient and it has only  $M$  non-zero eigenvalues, with the corresponding eigenvectors  $V_m(\omega)$ ,  $m = 1, \dots, M$ . When the scatterers are well resolved, the columns of the matrix  $\Gamma(\omega)$  are approximately orthogonal to each other, and the eigenvectors can be back-propagated as  $g^T(r, \omega)V_m(\omega)$ , and consequently the radiated wavefields focus at target locations. Thus, each eigenvector can be used to locate a single scatterer. For example, let us consider a scenario consisting of  $N = 100$  transceivers, separated by  $d = \lambda/2$ , and located at  $x_n = [0 \quad n\lambda/2 + a/2 - N\lambda/4]^T$ . Also, there are two targets,  $M = 2$ , with the scattering coefficients  $\rho_{1,2} = 1$ , situated at  $y_1 = [0.65 \quad 0.25]^T a$ , and respectively  $y_2 = [0.80 \quad 0.75]^T a$ . Here,  $a = 100\lambda$  is the side of the imaging area, and the computational image grid is set to  $L \times L = 200 \times 200$  pixels. In Figure 2 we give the first two back-propagated eigenvectors and the computed time-reversal image. One can see that since the targets are well separated the computed time-reversal image is almost a perfect superposition of the two independently back-propagated eigenvectors.

## 4 Subspace-based imaging

The above result does not apply to the case of poorly-resolved targets. In this case, the eigenvectors of  $K(\omega)$  are linear combinations of the target Green function vectors  $g(y_m, \omega)$ . Thus, back-propagating one of these eigenvectors generates a linear combination of wavefields, each focused on a different target location. The subspace-based algorithms, based on the multiple signal classification (MUSIC) method, can be used in this more general situation [7-9]. The signal subspace method assumes that the number  $M$  of point targets in the medium is lower than the number of transceivers  $N$ , and the general idea is to localize multiple sources by exploiting the eigenstructure and the rank deficiency of the response matrix  $H(\omega)$ .

The singular value decomposition of the symmetrical matrix  $H(\omega)$  is given by:

$$H(\omega) = U(\omega)\Lambda(\omega)V^*(\omega), \quad (22)$$

where  $U(\omega)$  and  $V(\omega)$  are the  $N \times N$  orthogonal matrices corresponding to the left and right singular vectors ( $V(\omega) = \overline{U}(\omega)$ , since  $H(\omega)$  is symmetric). The singular value matrix  $\Lambda(\omega)$  is diagonal  $\Lambda(\omega) = \text{diag}\{\lambda_1(\omega), \dots, \lambda_N(\omega)\}$ , and since  $H(\omega)$  is rank-deficient, all but the first  $M$  singular values vanish:

$$\lambda_i(\omega) \neq 0, \quad i = 1, \dots, M, \quad (23)$$

$$\lambda_j(\omega) = 0, \quad j = M + 1, \dots, N. \quad (24)$$

Therefore, the first  $M$  columns (singular vectors) of  $V(\omega)$  span the same subspace  $\sigma$  as the columns of  $\Gamma(\omega)$ , while the remaining  $N - M$  columns span the null-subspace  $\nu$  of  $\Gamma(\omega)$ . Thus, by partitioning  $V(\omega)$  as:

$$V(\omega) = [ V_\sigma(\omega) \quad V_\nu(\omega) ] \quad (25)$$

where  $V_\sigma(\omega)$  has the first  $M$  columns and  $V_\nu(\omega)$  has the remaining  $N - M$  columns, one can write the signal space as a direct sum  $\sigma \oplus \nu$ , where the essential signal-subspace  $\sigma$  is orthogonal to the null-subspace  $\nu$ . It follows immediately that:

$$V_\nu^*(\omega)H(\omega) = 0, \quad (26)$$

and therefore

$$V_\nu^*(\omega)g(r, \omega) = 0, \quad (27)$$

for any  $\omega$ . Therefore, the target locations must correspond to the peaks in the MUSIC pseudo-spectrum for any  $\omega$ :

$$P_{MUSIC}(r, \omega) = \|V_\nu^*(\omega)g(r, \omega)\|^{-2}, \quad (28)$$

where  $g(r, \omega)$  is the free-space Green function vector. Thus, one can form an image of the scatterers by plotting, at each point  $r$ , the quantity  $P_{MUSIC}(r, \omega)$ . The resulting plot will have large peaks at the locations of the scatterers. For example, let us consider a two dimensional scenario, consisting of  $N = 100$  linearly distributed transceivers, separated by  $d = \lambda/2$  and located at  $x_n = [ 0 \quad n\lambda/2 + a/2 - N\lambda/4 ]^T$ , where  $a = 100\lambda$  is the side of the imaging area. Also, there are  $M = 5$  targets with the scattering coefficients  $\rho_m = 10$ ,  $m = 1, \dots, M$ . The computational image grid is set to  $L \times L = 200 \times 200$  pixels. We consider two cases, one without noise, and the second one with Gaussian noise added to the elements of the response matrix  $H_{ij}(\omega)$ . The noise level was set such that the signal to noise ratio (SNR) is  $SNR = 2$ . SNR compares the level of a desired signal to the level of background noise. The higher the ratio, the less obtrusive the background noise is. SNR measures the power ratio between a signal and the background noise:

$$SNR = P_{signal}/P_{noise} = (A_{signal}/A_{noise})^2, \quad (29)$$

where  $P$  is average power and  $A$  is root mean square (RMS) amplitude. In Figure 3 we give the results obtained with the MUSIC algorithm in both cases. One can see that the MUSIC pseudo-spectrum provides a better resolution and separation of the targets, comparing to the back-propagation method.

## 5 Sparse approximation problem

The MUSIC algorithm provide very good resolution and separation of targets, however it cannot be used to quantify the properties of the targets, such as the magnitude of their scattering coefficients. Here we show that, with a little more

computational effort, we can also determine the scattering coefficients using a sparse image reconstruction approach.

Let us assume that the imaging domain is discretized as a grid of  $L^D$  voxels (pixels), and  $r_l$ ,  $l = 1, \dots, L^D$ , gives the position of each voxel. Also, we assume that  $\tilde{\rho}_l(\omega)$ ,  $l = 1, \dots, L^D$ , is the scattering factor associated with each voxel in the imaging domain. The goal is to find a matrix

$$\tilde{H}(\omega) = \sum_{l=1}^{L^D} \tilde{\rho}_l(\omega) g(r_l, \omega) g(r_l, \omega)^T, \quad (30)$$

which best approximates the response matrix  $H(\omega)$ :

$$\tilde{H}(\omega) \simeq H(\omega). \quad (31)$$

The above equation can be rewritten as:

$$\Phi(\omega) \tilde{\rho}(\omega) \simeq \Theta(\omega), \quad (32)$$

where  $\tilde{\rho}(\omega)$  is the unknown  $L^D$ -dimensional vector:

$$\tilde{\rho}(\omega) = [\tilde{\rho}_1(\omega), \dots, \tilde{\rho}_{L^D}(\omega)]^T. \quad (33)$$

The  $N^2$ -dimensional vector  $\Theta(\omega)$  is obtained by stacking the columns

$$H_n(\omega) = [ H_{1n}(\omega) \quad \dots \quad H_{Nn}(\omega) ]^T$$

of the response matrix  $H(\omega)$ :

$$\Theta(\omega) = [ H_{11}(\omega) \quad \dots \quad H_{N1}(\omega) \quad \dots \quad H_{1N}(\omega) \quad \dots \quad H_{NN}(\omega) ]^T. \quad (34)$$

Also,  $\Phi(\omega)$  is a matrix with  $N^2$  rows and  $L^D$  columns. Each column  $\Phi_l(\omega)$ ,  $l = 1, \dots, L^D$ , is obtained in a similar way, by stacking the columns of the  $N \times N$  matrix  $g(r_l, \omega) g(r_l, \omega)^T$ .

The above system of equations is underdetermined, since the number of scattering targets  $M$  is much smaller than  $L^D$ . The common approach to find a solution is to consider the equivalent  $l_2$ -optimization problem [11]:

$$\tilde{\rho}(\omega) = \arg \min_{\tilde{\rho}(\omega)} \|\tilde{\rho}(\omega)\|_2 \quad s.t. \quad \Phi(\omega) \tilde{\rho}(\omega) = \Theta(\omega), \quad (35)$$

where  $\|\tilde{\rho}(\omega)\|_2 = \sqrt{\sum_{l=1}^{L^D} |\tilde{\rho}_l(\omega)|^2}$ , is the Euclidean norm. In this case, the unique solution which minimizes the  $l_2$ -norm, is given by:

$$\tilde{\rho}(\omega) = \Phi^\dagger(\omega) \Theta(\omega), \quad (36)$$

where

$$\Phi^\dagger(\omega) = [\Phi^*(\omega) \Phi(\omega)]^{-1} \Phi^*(\omega), \quad (37)$$

is the More-Penrose pseudoinverse of the matrix  $\Phi(\omega)$ . However, in this case all the coefficients of the solution  $\tilde{\rho}(\omega)$  are non-zero, and therefore, this solution is not in agreement with the fact that the imaging region is sparse, i.e. the number of scattering targets is  $M \ll L^D$ . Therefore, this is not the correct solution of the approximation problem. In fact, we would like to find the minimum number of columns  $\Phi_l(\omega)$  of  $\Phi(\omega)$  which approximate the data vector  $\Theta(\omega)$ . This is a sparse approximation problem, and as a measure of sparsity we consider the  $l_0$  norm of  $\tilde{\rho}(\omega)$ ,  $\|\tilde{\rho}(\omega)\|_0$ , which simply counts the number of nonzero coefficients in the vector  $\tilde{\rho}(\omega)$ . These non-zero coefficients will give the position, and their magnitude will reflect the value, of the scattering coefficients of the targets in the  $L^D$  imaging region. Thus, the sparsest representation requires the solution of the  $l_0$ -optimization problem [12]:

$$\tilde{\rho}(\omega) = \arg \min_{\tilde{\rho}(\omega)} \|\tilde{\rho}(\omega)\|_0 \quad s.t. \quad \Phi(\omega)\tilde{\rho}(\omega) = \Theta(\omega). \quad (38)$$

Unfortunately, this combinatorial optimization problem is NP-hard to solve, requiring the enumeration of all possible collections of columns in  $\Phi(\omega)$  and searching for the smallest collection which best approximates the data vector  $\Theta(\omega)$ . An alternative is the convexification of the objective function, which is obtained by replacing the  $l_0$  norm with the  $l_1$  norm:  $\|\tilde{\rho}(\omega)\|_1 = \sum_{l=1}^{L^D} |\tilde{\rho}_l(\omega)|$ . The resulting  $l_1$ -optimization problem:

$$\tilde{\rho}(\omega) = \arg \min_{\tilde{\rho}(\omega)} \|\tilde{\rho}(\omega)\|_1 \quad s.t. \quad \Phi(\omega)\tilde{\rho}(\omega) = \Theta(\omega) \quad (39)$$

is known as Basis Pursuit (BP), and it can be solved using linear programming techniques whose computational complexities are polynomial [12]. The BP method recasts the  $l_1$ -problem as a linear program, and it has been shown that because of the nondifferentiability of the  $l_1$  norm, this optimization problem leads to unique sparse solutions. However, the BP approach requires the solution of a very large convex, nonquadratic optimization problem, and therefore still suffers from high computational complexity. For example in a three dimensional problem,  $D = 3$ , with  $N = 100$  transceivers and a discretization grid with  $L = 100$ , the resulted dimensionality of the  $\Phi(\omega)$  matrix is:  $10^4 \times 10^6$ , and the number of unknowns in the vector  $\tilde{\rho}(\omega)$  is  $10^6$ . As an alternative, here we consider a heuristic approach based on iterative greedy algorithms, which also have been proven to give good approximative solutions to the sparse reconstruction problem.

## 6 Greedy algorithm for sparse approximation

Matching Pursuit (MP) is a general procedure to compute adaptive signal representations and to extract the signal structure in a given time-frequency dictionary [13]. Also, it has been shown that the MP algorithm can be used to obtain (approximative) sparse solutions of the  $l_0$ -optimization problem [14-16].



Although the MP algorithm is non-linear, it maintains an energy conservation which guarantees its convergence.

In the case of computational time-reversal imaging, the elements of the time-frequency dictionary are given by the columns  $\Phi_l(\omega)$  of the matrix  $\Phi(\omega)$ . Using this dictionary, the data vector  $\Theta(\omega)$  can be represented as:

$$\Theta(\omega) = \sum_{l=1}^{L^D} \tilde{\rho}_l(\omega) \Phi_l(\omega). \quad (40)$$

The vector  $\Theta(\omega)$  can be decomposed into:

$$\Theta(\omega) = [\Phi_l^*(\omega)\Psi(\omega)] \|\Phi_l(\omega)\|^{-2} \Phi_l(\omega) + \Psi(\omega), \quad (41)$$

where  $\Psi(\omega)$  is the residual vector after approximating  $\Theta(\omega)$  in direction of  $\Phi_l(\omega)$ . Since  $\Phi_l(\omega)$  and  $\Psi(\omega)$  are orthogonal, we have:

$$\|\Psi(\omega)\|^2 = \|\Theta(\omega)\|^2 - |\Phi_l^*(\omega)\Theta(\omega)|^2 \|\Phi_l(\omega)\|^{-2}, \quad (42)$$

and in order to minimize  $\|\Psi(\omega)\|$  we must choose the column  $\Phi_l(\omega)$ , such that  $|\Phi_l^*(\omega)\Theta(\omega)| \|\Phi_l(\omega)\|^{-1}$  is maximum. Thus, starting from an initial approximation  $\tilde{\rho}(\omega) = 0$  and a residual  $\Psi(\omega) = \Theta(\omega)$ , the algorithm uses an iterative greedy strategy to pick the columns  $\Phi_l(\omega)$  of  $\Phi(\omega)$  that are the most strongly correlated with the residual. Then, successively their contribution is subtracted from the residual, which this way can be made arbitrarily small. The pseudo-code of the MP algorithm is:

1. Initialize the variables:

$$T, t \leftarrow 1, \tilde{\rho}(\omega) \leftarrow 0, \Psi(\omega) \leftarrow \Theta(\omega). \quad (43)$$

2. Find  $l$  such that:

$$l = \arg \max_{l=1, \dots, L^D} |\Phi_l^*(\omega)\Psi(\omega)| \|\Phi_l(\omega)\|^{-1}. \quad (44)$$

3. Update the estimate of the corresponding coefficient, the residual, and the iteration counter:

$$\tilde{\rho}_l(\omega) \leftarrow \tilde{\rho}_l(\omega) + [\Phi_l^*(\omega)\Psi(\omega)] \|\Phi_l(\omega)\|^{-2}, \quad (45)$$

$$\Psi(\omega) \leftarrow \Psi(\omega) - [\Phi_l^*(\omega)\Psi(\omega)] \|\Phi_l(\omega)\|^{-2} \Phi_l(\omega), \quad (46)$$

$$t \leftarrow t + 1. \quad (47)$$

4. If  $\|\Psi(\omega)\|^2 < \varepsilon \|\Theta(\omega)\|^2$  or  $t > T$  then terminate and return  $\tilde{\rho}(\omega)$ . Otherwise go to 2.

The stopping criterion in the step 4 requires the residual to be smaller than some fraction  $0 < \varepsilon \ll 1$  of the data vector. Also, the computation stops if the number of iterations exceed the maximum number allowed  $T$ . Although the asymptotic convergence of MP algorithm can be easily proven, the resulting approximation after any finite number of steps will in general be suboptimal. In the case of noise, the MP algorithm is used to obtain an approximative sparse solution by simply stopping the iteration when the projection of the residual on the chosen direction  $\Phi_l(\omega)$  becomes smaller than a threshold  $0 < \tau < 1$  [14-16]. Thus, in the case of noise, the MP algorithm is modified simply by replacing the stopping condition with:  $|\Phi_l^*(\omega)\Psi(\omega)|^2 \|\Phi_l(\omega)\|^{-2} \|\Psi(\omega)\|^{-2} < \tau$ . After the computation is finished, the image is formed by plotting  $\tilde{\rho}_l(\omega)$  at location  $r_l$ ,  $l = 1, \dots, L^D$ . We should note that the algorithm works in both cases, when  $\rho_l(\omega)$  is complex, or when only its magnitude  $|\rho_l(\omega)|$  is given. In the later case, one should plot the absolute values of the computed coefficients  $|\tilde{\rho}_l(\omega)|$ .

## 7 Implementation and numerical results

It is important to note that one can implement the MP algorithm such that the elements of the matrix  $\Phi$  do not need to be stored. In fact, one can compute the columns  $\Phi_l$  of  $\Phi$  at every step of the algorithm, since the Green function is known. Thus, the algorithm requires only operations with vectors of length  $N^2$ , which is feasible on standard personal computers. However, since the number of vector-vector multiplications per iteration step is high,  $L^2$ , a parallel implementation of the algorithm is desirable. We have implemented the MP algorithm for the NVIDIA GPU (Graphics Processing Unit) platform. Recently, NVIDIA has released a general purpose oriented API for its graphics hardware, called CUDA [17]. In addition, NVIDIA has developed CUBLAS which is a GPU optimized version of BLAS library (Basic Linear Algebra Subroutines) built on top of CUDA [18]. The newly developed GPUs now include fully programmable processing units that follow a stream programming model and support vectorized single and double precision floating-point operations. For example, the CUDA computing environment provides a standard C like language interface to the NVIDIA GPUs. The computation is distributed into sequential grids, which are organized as a set of thread blocks. The thread blocks are batches of threads that execute together, sharing local memories and synchronizing at specified barriers. CUBLAS library provides functions for: (i) creating and destroying matrix and vector objects in GPU memory; (ii) transferring data from CPU mainmemory to GPU memory; (iii) executing BLAS on the GPU; (iv) transferring data from GPU memory back to the CPU mainmemory. CUBLAS defines a set of fundamental operations on vectors and matrices which can be used to create optimized higher-level linear algebra functionality: (i) Level 1 BLAS perform scalar, vector and vector-vector operations; (ii) Level 2 BLAS perform matrix-vector operations; (iii) Level 3 BLAS perform matrix-matrix operations. However, in its current version CUBLAS does not offer direct support for operations involving vectors and matrices of complex numbers. In the

case of the MP algorithm, one can easily overcome this drawback by storing separately the real and imaginary part of the vectors and matrices. This way, complex vector-vector and matrix-vector operations can be reduced to operations involving only real numbers. The parallel implementation of the MP algorithm requires only Level 1 or Level 2 (if  $\Phi$  is stored) BLAS operations. Our numerical tests have shown that the parallel GPU implementation versus a standard CPU BLAS implementation of the MP algorithm reaches a speed up of a maximum of 31 times in single precision and respectively 21 times in double precision [19].

Let us now consider a two dimensional scenario, consisting of  $N = 100$  linearly distributed transceivers, separated by  $d = \lambda/2$  and located at  $x_n = [0 \quad n\lambda/2 + a/2 - N\lambda/4]^T$ , where  $a = 100\lambda$  is the side of the imaging area. The computational image grid was also set to  $L \times L = 100 \times 100$ . This scenario will generate a dictionary  $\Phi$  of size  $N^2 \times L^2 = 10^4 \times 10^4$  and an unknown vector  $\tilde{\rho}$  of size  $N^2 = 10^4$ . The number of targets is set to  $M = 5$  and their position is randomly generated in the imaging area. The scattering coefficients are generated randomly from a uniform distribution such that  $1 \leq \rho_m \leq 10$ ,  $m = 1, \dots, M$ . We consider both cases, with and without noise. The signal to noise level is set to  $SNR = 2$ , as for the described MUSIC algorithm case.

First, let us discuss the case without noise. The threshold parameter and the maximum number of iterations were set to  $\varepsilon = 10^{-4}$ , and respectively  $T = N$ . In Figure 4 we give the initial and the computed arrangement of the targets, and their initial and computed values of the scattering coefficients. One can see that the agreement between the initial values and the computed ones is very good, and the MP algorithm can solve the problem almost perfectly. In Figure 5 we give the real and imaginary part of the initial and reconstructed response matrix. The error is less than 1% in both cases. Also, Figure 6 shows the computed image using the MP algorithm. One can see that the peaks are very sharp and their position and amplitude reflects correctly the initial position and the magnitude of the scattering coefficients. This example shows that the MP algorithm can solve almost perfectly (in the limits of the image resolution) the computational time-reversal imaging problem if the response matrix is not affected by noise.

Let us consider the case with noise, using the same arrangement of the targets, with the same values for the scattering coefficients. In this case the threshold  $\tau$  plays a very important role in the MP algorithm. We consider two different values  $\tau = 10^{-3}$  and  $\tau = 10^{-2}$ . In Figure 7 we give the real and the imaginary part of the initial and reconstructed response matrix. One can see that the reconstructed response matrix contains a much lower amount of noise than the original response matrix. Also, by increasing the value of  $\tau$ , the amount of noise in the reconstructed response matrix decreases dramatically. This can be seen also on the computed images, given in Figure 8. The amount of noise in the computed images is very small, given the  $SNR = 2$  level in the perturbed response matrix. Also, the position of the peaks, corresponding to the targets, and their magnitude are still very well maintained. This means that the sparse

approximation, given by the MP algorithm, and the threshold parameter  $\tau$ , acts as a denoising method, and respectively as a denoising parameter, and it can be successfully used in computational time-reversal imaging.

## 8 Conclusion

We have presented a sparse approximation method for computational time-reversal imaging. The method is formulated entirely in the frequency domain, and it is based on an adapted version of the matching pursuit algorithm, which can be successfully used to compute an accurate sparse approximation of the frequency response matrix. This approach can be used for denoising the computed time-reversal images, and to determine the magnitude of the scattering coefficients of the targets embedded in homogeneous media, in the presence of moderate to high noise levels. Also, in comparison to the back-propagation and the null subspace projection methods, the described approach provides a better resolution. However, the sparse approximation method is computationally more expensive than the traditional approaches.

## References

- [1] L. Borcea, G. Papanicolaou, C. Tsogka, J. Berryman, Imaging and time reversal in random media, *Inverse Problems*, 18 (2002) 1247.
- [2] M. Fink, D. Cassereau, A. Derode, C. Prada, P. Roux, M. Tanter, J.-L. Thomas and F. Wu, *Reports on Progress in Physics* 63 (2000) 1933.
- [3] C. Prada, E. Kerbrat, D. Cassereau, M. Fink, Time reversal techniques in ultrasonic nondestructive testing of scattering media, *Inverse Problems*, 18 (2002) 1761.
- [4] C. Prada, L. Thomas, M. Fink, The Iterative Time Reversal Process: Analysis of the Convergence, *Journal of the Acoustical Society of America*, 97 (1995) 62.
- [5] C. Prada, M. Fink, Eigenmodes of the time reversal operator: A solution to selective focusing in multiple-target media, *Wave Motion*, 20 (1994) 151.
- [6] C. Prada, S. Manneville, D. Spoliansky, M. Fink, Decomposition of the Time Reversal Operator: Detection and Selective Focusing on Two Scatterers, *Journal of the Acoustical Society of America*, 99 (1996) 2067.
- [7] F.K. Gruber, E.A. Marengo, A.J. Devaney, Timereversal imaging with multiple signal classification considering multiple scattering between the targets, *Journal of the Acoustical Society of America*, 115 (2004) 3042.
- [8] E.A. Marengo, F.K. Gruber, Subspace-Based Localization and Inverse Scattering of Multiply Scattering Point Targets, *EURASIP Journal on Advances in Signal Processing*, (2007) Article ID 17342.

- [9] H. Lev-Ari, A. J. Devaney, The time-reversal technique reinterpreted: Subspace-based signal processing for multi-static target location, IEEE Sensor Array and Multichannel Signal Processing Workshop, Cambridge (MA), USA, (2000) 509.
- [10] J. H. Taylor, Scattering Theory, Wiley, New York, 1972.
- [11] G. H. Golub, C. F. Van Loan, Matrix Computations. Johns Hopkins University Press, Baltimore, 1996.
- [12] S. S. Chen, D. L. Donoho, M. A. Saunders, Atomic decomposition by basis pursuit, SIAM Journal of Scientific Computing 20 (1998) 3361.
- [13] S. Mallat, Z. Zhang, Matching pursuit in a time-frequency dictionary. IEEE Transactions on Signal Processing 41 (1993) 3397.
- [14] D. L. Donoho, M. Elad, V. N. Temlyakov, Stable recovery of sparse over-complete representations in the presence of noise. IEEE Transactions on Information Theory, 52 (2006) 618.
- [15] M. Andrecut, S. Huang, S. A. Kauffman, Heuristic approach to sparse approximation of gene regulatory networks, Journal of Computational Biology 15(9) (2008) 1173 .
- [16] M. Andrecut, S. A. Kauffman, On the sparse reconstruction of gene networks, Journal of Computational Biology 15(1) (2008) 21 .
- [17] NVIDIA, Nvidia CUDA Compute Unified Device Architecture, Programming Guide, 2008.
- [18] NVIDIA, CUBLAS Library, 2008.
- [19] M. Andrecut, Fast GPU implementation of sparse signal recovery from random projections, Engineering Letters (to appear, 2009, arXiv:0809.1833), [www.nvidia.com/content/cudazone/CUDABrowser/assets/data/applications.xml](http://www.nvidia.com/content/cudazone/CUDABrowser/assets/data/applications.xml).

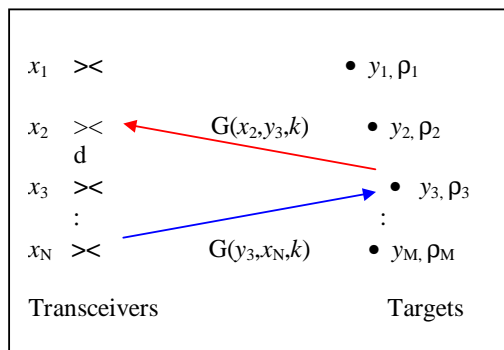


Figure 1: Geometry for the time-reversal imaging experiment, containing  $N$  transceivers and  $M$  scattering targets.

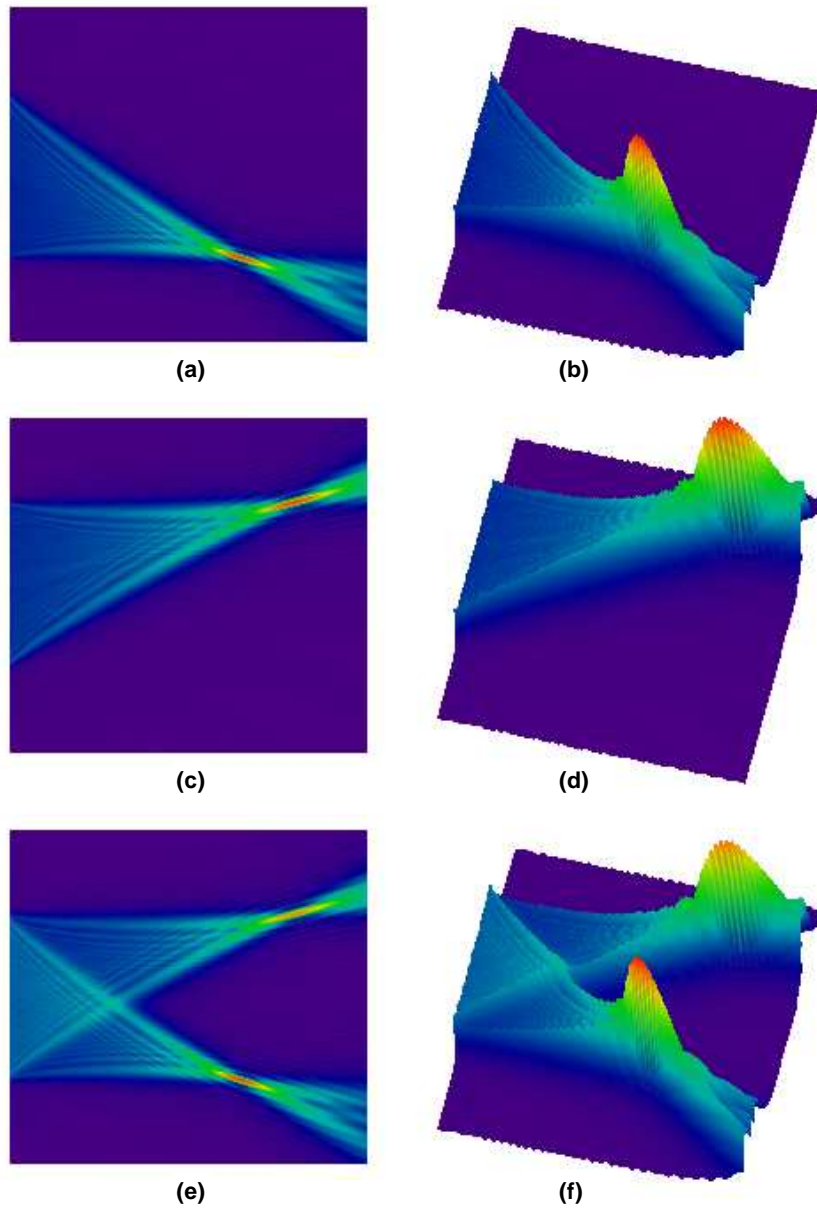


Figure 2: Time-reversal wavefields in the case of two targets: (a-b) the first eigenvector; (c-d) the second eigenvector; (e-f) the computed time-reversal image.

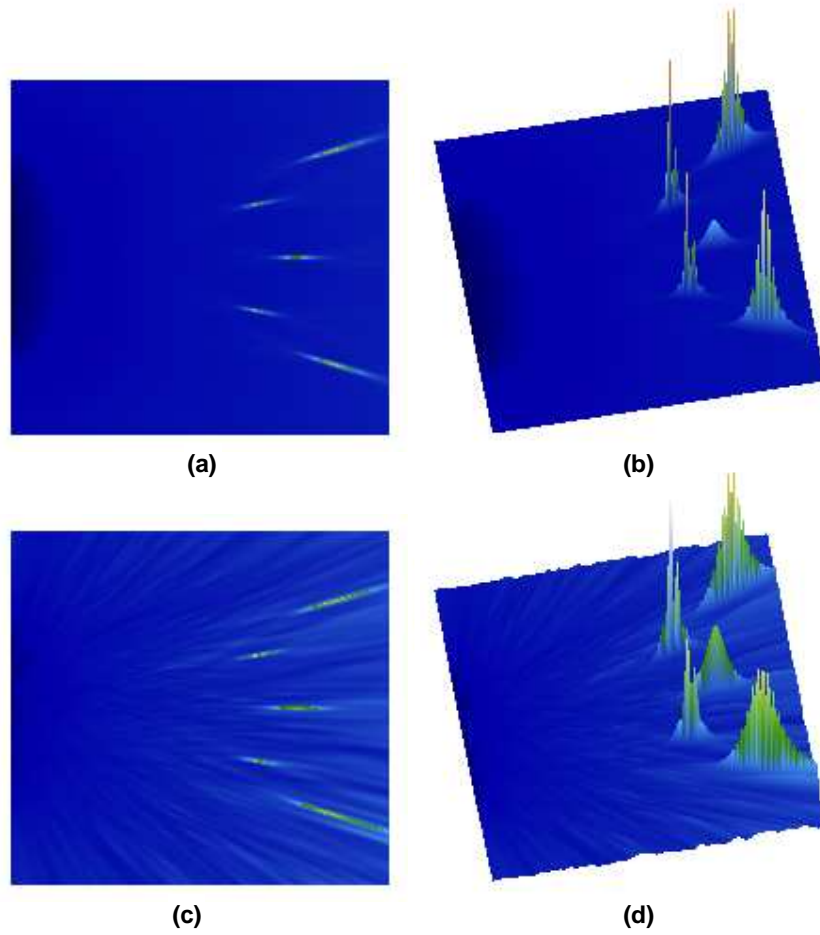


Figure 3: The MUSIC pseudo-spectrum in case of  $M = 5$  targets: (a-b) without noise; (c-d) with noise,  $SNR = 2$ .



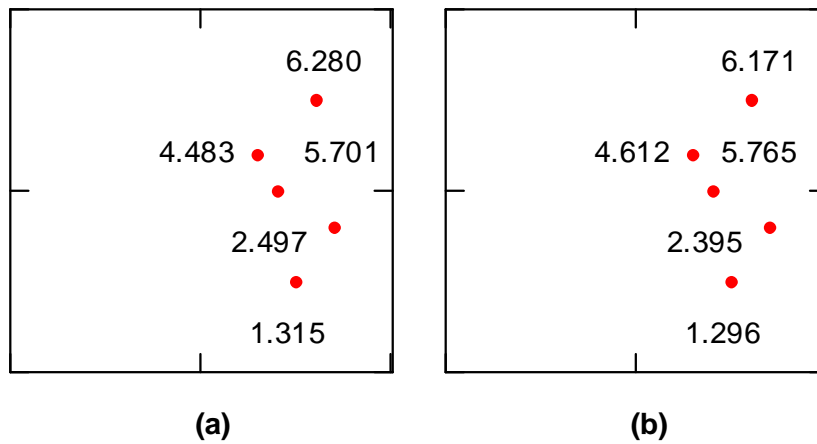


Figure 4: Sparse approximation of time-reversal image in case of  $M = 5$  targets: (a) the initial location of the targets and their scattering coefficients; (b) the computed location of the targets and their scattering coefficients.

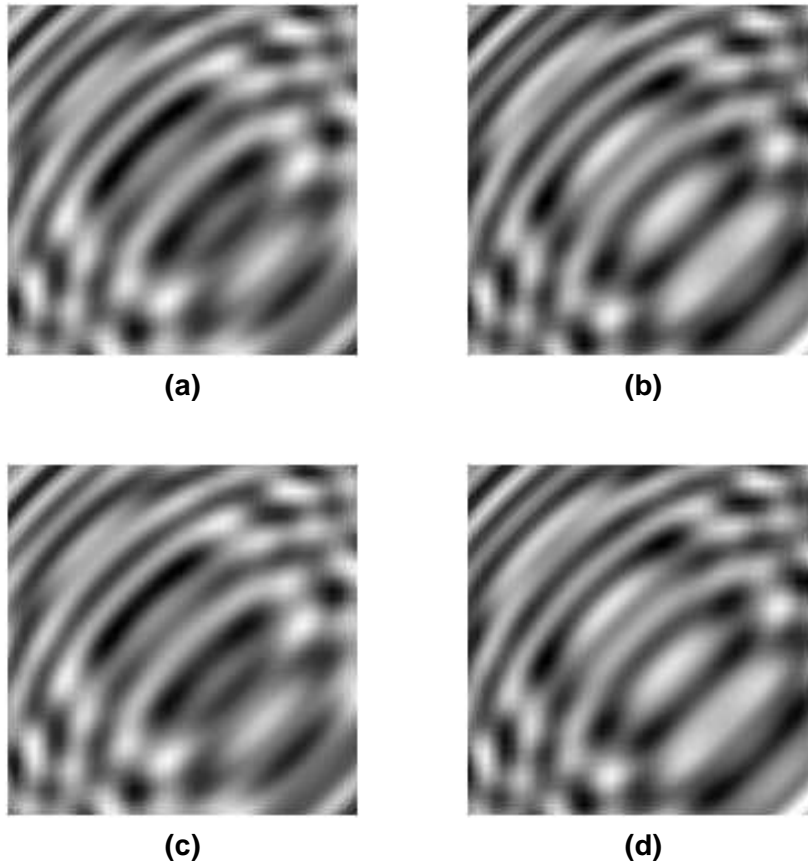


Figure 5: Sparse approximation of time-reversal image in case of  $M = 5$  targets, without noise: (a-b) the real and imaginary part of the initial response matrix; (c-d) the real and imaginary part of the computed response matrix.

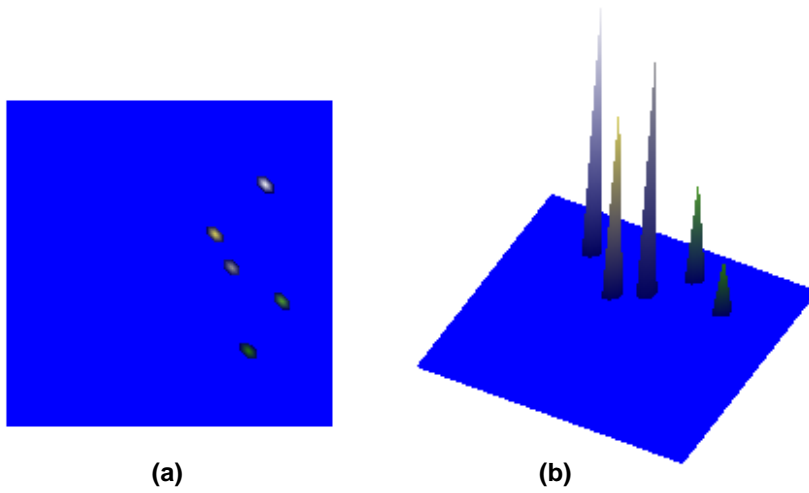


Figure 6: The computed time-reversal image, using the sparse approximation approach, in case of  $M = 5$  targets, without noise.

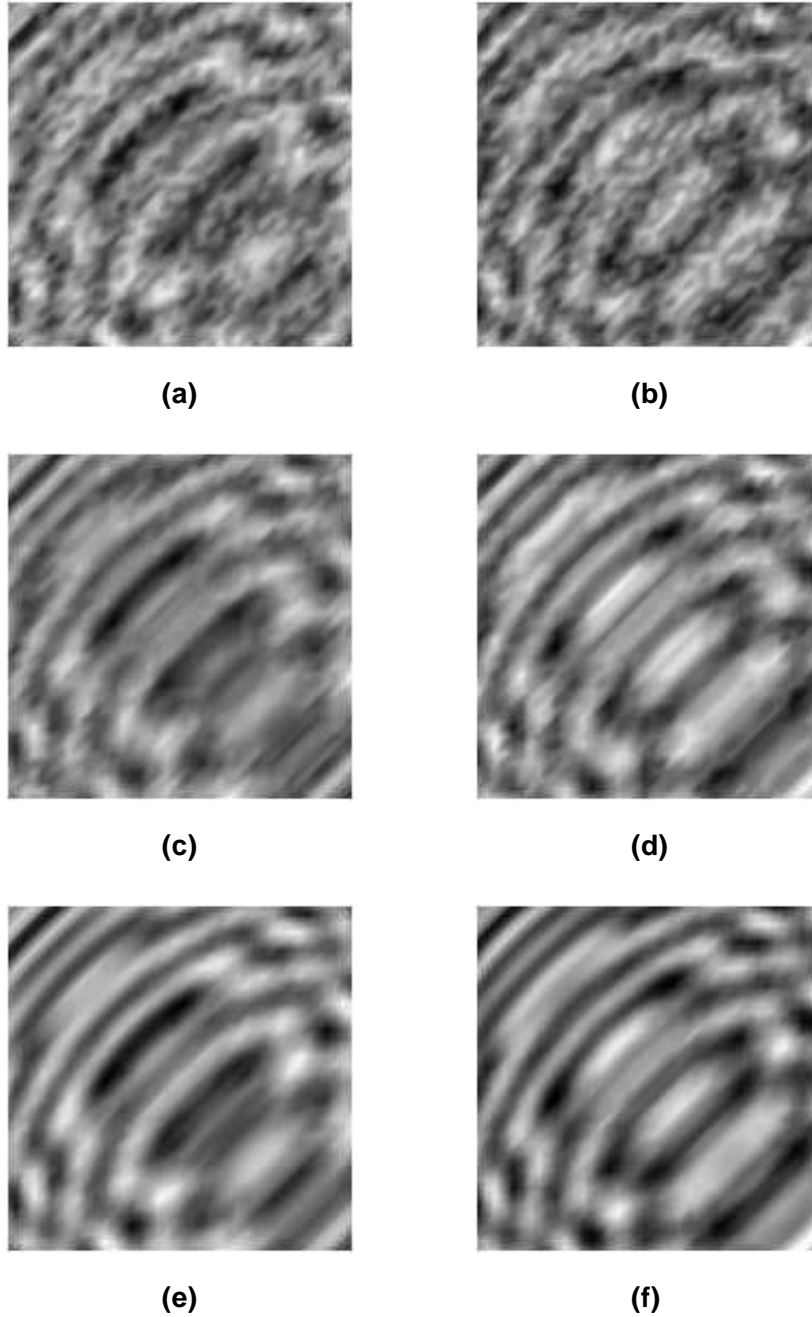
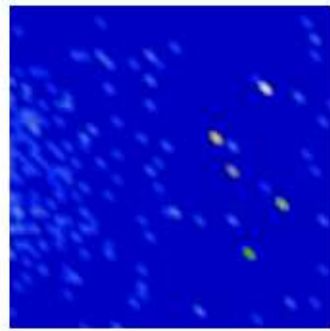
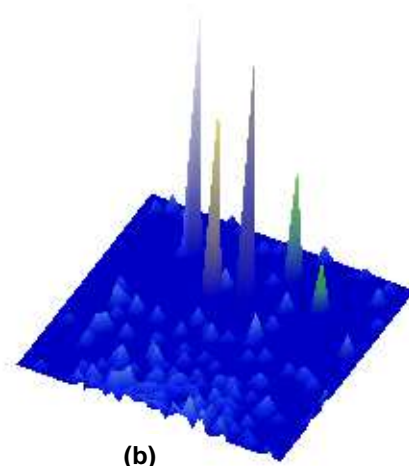


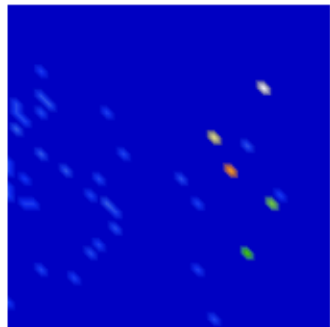
Figure 7: Sparse approximation of time-reversal image in case of  $M = 5$  targets, with noise: (a-b) the real and imaginary part of the initial response matrix with the noise level  $SNR = 2$ ; (c-d) the real and imaginary part of the computed response matrix with  $\tau = 10^{-3}$ ; (e-f) the real and imaginary part of the computed response matrix with  $\tau = 10^{-2}$ .



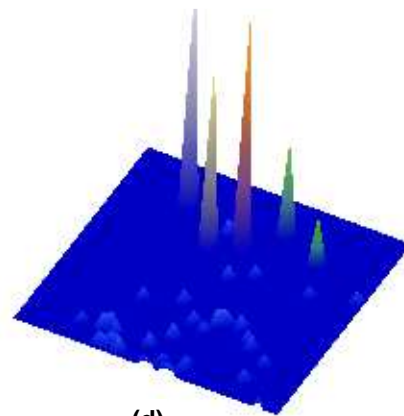
(a)



(b)



(c)



(d)

Figure 8: The computed time-reversal image, using the sparse approximation approach, in case of  $M = 5$  targets, with noise ( $SNR = 2$ ): (a-b)  $\tau = 10^{-3}$ ; (c-d)  $\tau = 10^{-2}$ .